NASA Technical Memorandum 103618
AIAA-90-2649

Status of Structural Analysis of 30 cm Diameter Ion Optics

Gregory S. MacRae and Gary T. Hering
Lewis Research Center
Cleveland, Ohio

Prepared for the
21st International Electric Propulsion Conference
cosponsored by the AIAA, DGLR, and JSASS
Orlando, Florida, July 18-20, 1990

NASA

STATUS OF STRUCTURAL ANALYSIS OF 30 CM DIAMETER ION OPTICS

Gregory S. MacRae and Gary T. Hering
National Aeronautics and Space Administration
Lewis Research Center
Cleveland, Ohio 44135

ABSTRACT

Three structural finite element programs are compared with theory, experimental data, and each other to evaluate their usefulness for modeling the thermomechanical deflection of ion engine electrodes. Two programs, NASTRAN and MARC, used a Cray XMP and the third, Algor, used an IBM compatible personal computer. The shape of the applied temperature gradient greatly affects off-axis displacement, implying that an accurate temperature distribution is required to analyze new designs. The use of bulk material constants to model the perforated electrodes was investigated. The stress and displacement predictions are shown to be sensitive to the temperature gradient and the Young's modulus, and insensitive to number of nodes, above some minimum value, and the Poisson ratio used. The models are shown to be useful tools for evaluating designs. Experimental measurement of temperatures and displacements was identified as the most critical area for further work.

NOMENCLATURE

A_s	surface area
C	1/2 the center to center hole spacing
d	effective acceleration distance
e	electron charge
E	Young's modulus
E*	adjusted Young's modulus
F_{max}	maximum thrust
h	instantaneous ligament half-thickness
h_m	mean ligament half-thickness
J_B	total beam current
$\tilde{K}$	global stiffness matrix
ℓ	distance along a ligament
L	hexagonal side length from hole pattern
M	atomic mass
n	ligament shape factor
$\hat{P}$	generalized force vector
R	outer radius of circular plate
r	radius
S	von Mises stress
s	path length
t	electrode thickness
T	temperature
$\hat{T}$	nodal temperature vector
$\hat{u}$	nodal displacement vector
V_n	net accelerating voltage
w	axial displacement
2D	two dimensional
3D	three dimensional
α	coefficient of thermal expansion
χ	Child's Law constant
ΔT	center to edge temperature change
γ	thrust correction factor for multiply charged ions and beam divergence
ν	Poisson ratio
ν^*	adjusted Poisson ratio
σ_a	stress in the axial direction
σ_c	stress in the circumferential direction
σ_r	stress in the radial direction

ACRONYMS

CPU	central processing unit
DEC	Digital Equipment Corporation
IBM	International Business Machines
PC	personal computer

INTRODUCTION

Ion engines can provide a specific impulse of 3000 to 8000 sec and thrusts of 0.1 to 1 N for systems with tens of kW available per engine.[1] Ion engines are very fuel efficient for many orbital applications, especially orbital transfer maneuvers and planetary missions.[2,3] Orbit transfers and planetary missions require scaling ion engines from tens of kW to MW powers for Mars transfer propulsion.

An ion engine accelerates charged particles via an electrostatic field that is maintained between two thin, perforated electrodes. The charged

particle exit velocity is determined by the accelerating voltage and the charge to mass ratio of the particle. The thrusters are normally operated near the current limit which is defined by Child's Law,

$$J_B = \frac{\chi A_s V_n^{3/2}}{d^2} \qquad (1)$$

where J_B is the total beam current and χ, sometimes called Child's Law constant, is primarily determined by geometry.[4] Converting the current to thrust gives,

$$F_{max} = \frac{\chi \gamma A_s V_n^2}{d^2} \sqrt{\frac{2M}{e}} \qquad (2)$$

where γ is a correction factor to account for doubly charged particles and beam divergence.[5] The detailed geometry of the electrodes, ie. hole size, hole alignment, electrode thickness, etc., modify the effective acceleration length, the Child's constant and the thrust correction factor. The contributions have been studied and are described in detail in references 4 through 7. In addition to optimizing the detailed geometry, the thrust per engine may be increased without affecting the specific impulse by reducing the electrode gap to reduce the effective acceleration distance or by increasing the beam extraction area of the engine.

If the gap is too small, arc discharges from the screen to the accelerator electrode may occur too frequently. When the electrode area is increased, the effect thermally induced motion has on the electrode gap must be examined. Methods considered for increasing the electrode area include scaling up current engine designs or redesigning with a non-circular axisymmetric shape[8] or a non-axisymmetric shape.[9] Initial attempts to scale from 30 to 50 cm diameter electrodes resulted in beam current densities significantly less than expectations based on extrapolations from 30 cm diameter thruster performance.[10] Non-circular electrode shapes provide a means of reducing the span to gap ratio of the electrodes while increasing the area, but they also diverge from the designs which have large design and operational experience data bases. Computer modeling provides the potential to quickly analyze new designs and build the data base necessary to implement them.

Structural analyses of ion engines have been conducted by a number of ion propulsion technologists.[11-13] Models of two and three electrode systems were developed. All three of the modeling efforts cited used experimental data to confirm portions of the models. None of the models addressed non-linear effects of geometry and material properties.

The goal of modeling efforts at Lewis Research Center is to verify and expand current modeling methods. This includes: checking the codes against theoretical and experimental data, documenting and justifying the selection of mesh elements and geometry, and verifying the non-linear modeling capabilities of the software. Toward these ends, models were built on three different finite element codes to analyze the structure of the electrode assembly. Comparisons were made within each code to evaluate model structures. Models from different codes were compared with each other and with plate-shell theory analysis to evaluate accuracy. Experimental measurements were compared with code predictions to evaluate the limitations and effectiveness of the modeling. The ability of all three software packages to handle non-linear effects was verified through a literature search.[14-16] The non-linear capabilities are required for modeling of non-axisymmetric electrodes, plastic strains, temperature variable and non-isometric material properties, and manufacturing defects. The intent of this paper is to describe the method and results of using finite element programs to model thermally induced motion of ion engine electrode assemblies.

APPARATUS

Study of the structural response of ion engines involves models to predict stresses and deformations, and experimental evaluation of temperatures and deformations. Three commercially available software packages were used to model the ion engine. The major code characteristics are described herein and summarized in Table I. The temperature and displacement measurements were described in a previous report,[17] so only an overview will be given here.

Code Descriptions

Three different finite element, structural analysis codes were used to model thermally induced stress and deflection of ion engine electrodes. The codes were chosen because they were available and all support 3D Cartesian, 2D axisymmetric, and non-linear material and geometry effects analyses.

The general operation of the codes is similar. A finite element model of the structure to be analyzed is generated

TABLE I: COMPARISON OF CODES USED.

Processors				Non-Linear		2D		Temperature	Data
Main	Pre-	Post-	CPU	Materials	Displacement	Axisymmetric	3D	Definitions	Report Positions
Algor	Algor	Algor	IBM PC	✓	✓	✓	✓	pre-processor	nodes
MARC	PATRAN	PC	Cray	✓	✓	✓	✓	main processor	integration points
NASTRAN	PATRAN	PC	Cray	✓	✓	✓	✓	pre-processor	centroids

using a pre-processor. Displacement boundary conditions are applied using a combination of the pre-processor and a text editor. Each code used a different method to apply the thermal data. The main processor then assembles a global stiffness matrix using the data, and solves Hooke's Law, modified to account for thermal strain,

$$\hat{P}=\hat{K}(\hat{u}-\alpha\hat{T}). \qquad (3)$$

Displacement, stress, and temperature predictions are generated and written to a file. Each code generates data differently. A post-processor is used to display and compare the results generated by the different codes.

A general description of each codes capabilities and specific characteristics follows, the detailed modeling approach will be discussed in the next section.

Algor This code is written for an IBM compatible PC with a math co-processor.[14] It is written in a modular fashion, with separate programs for pre- and post-processing, stiffness matrix generation, thermal analysis, buckling analysis, static stiffness matrix solution, and dynamic mass and stiffness solution. Each individual routine has a unique name. For simplicity, the collection of programs will be referred to as Algor. Temperature effects are applied through the pre-processor. Data is generated at the element nodes. The output files from the separate routines can be used as input for the related routines, eg. the output from a thermal analysis can be applied as part of the load condition for a structural analysis, allowing one to restart a simulation from almost any previous solution. Only the pre- and post-processor and the elements necessary for static structural analysis in 3D and axisymmetric 2D have been used to date. Additional post processing was done using several personal computer spreadsheet and graphing packages.

MARC This code is written and supported by the MARC Analysis Research Corporation, and works on a variety of machines, including mainframes by Cray Research, DEC, and IBM.[18] The program supports thermal, buckling, static structural and dynamic structural analyses. Temperature conditions were applied at the solution time through a user written subroutine. Data are reported for integration points within each element. As with the Algor package, restart files can be written from any point in the analysis and data from thermal analyses can be used as input for stress analyses. Again, this feature was not tested. At LeRC, MARC is installed on a Cray XMP. Pre-processing was done entirely with PATRAN,[19] a separate program running on a VAX computer. Post-processing was done with PATRAN and several personal computer spreadsheet and graphing packages.

NASTRAN This code is widely known, in part because several versions exist. A version supported by the MacNeal-Schwendler Corporation was installed on a Cray XMP.[20] The program supports thermal, buckling, static structural, dynamic structural and limited fluid flow analyses. Only the static stress analysis solution set was used. Thermal conditions were applied to the nodes by editing the input file. Data are generated at the centroids of the elements. Pre- and post-processing were identical to that used for MARC, excepting the different report formats used by the two codes.

Hardware Description

Because some of the model predictions will be compared with ion engine data, a brief description of the ion extraction system as well as hardware used to measure temperatures and deflections is presented. The testing described was completed in 1981 and is described more completely in reference 17.

The experimental tests were conducted using a J-series electrode assembly mounted on a 30 cm diameter divergent field ion thruster. The J-series assemblies were fabricated in the late 1970's for planetary propulsion applications using mercury propellant at 3 kW power levels.[21] A typical thruster is shown in Fig. 1. The engine body is 26 cm long and 34.6 cm in diameter, with a cathode protruding 4 cm into the chamber, along the centerline. The plasma discharge is the main source of thermal input to the electrodes. An estimated 10 percent of the discharge power is radiated through the electrodes.[22] The two electrode, J-series assembly is shown in Fig. 2. It consists of six basic parts: a titanium mounting ring which attaches to the plasma discharge chamber, the positively charged screen electrode which faces the plasma, a negatively charged extraction or accelerator electrode, a set of insulators which provide electrical isolation between the screen and accelerator electrodes,

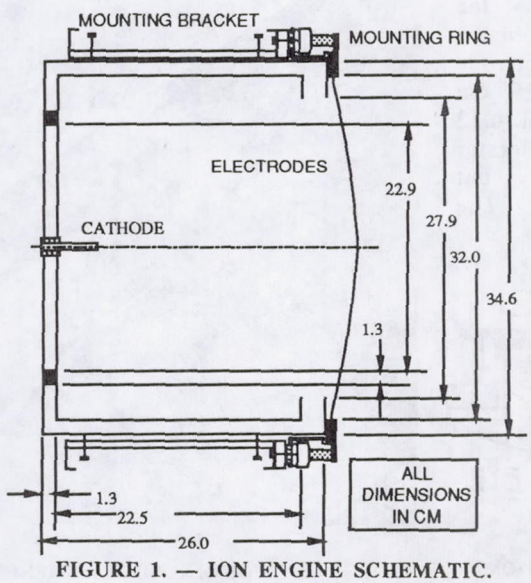

FIGURE 1. — ION ENGINE SCHEMATIC.

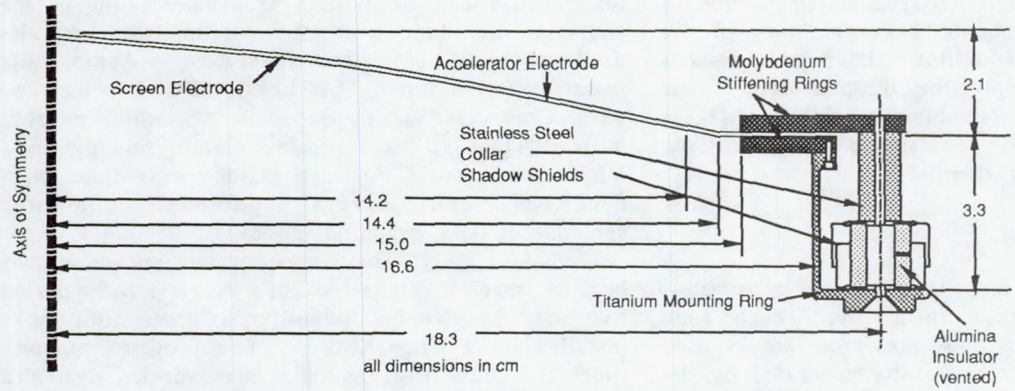

FIGURE 2.— J-SERIES ELECTRODE ASSEMBLY CROSS SECTION.

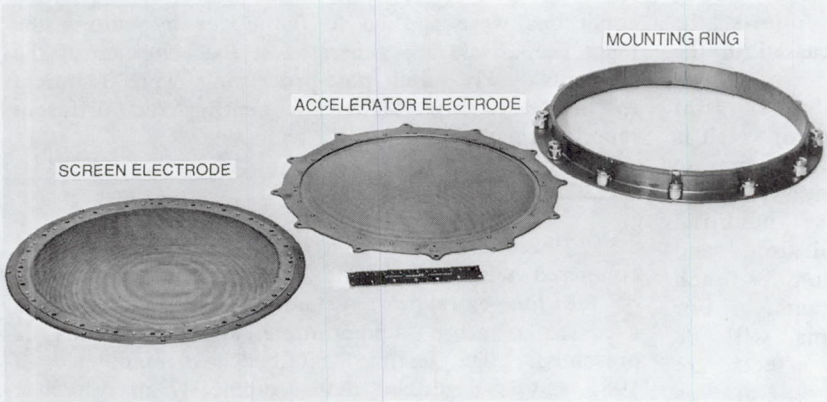

FIGURE 3.— J-SERIES ELECTRODE ASSEMBLY COMPONENTS.

and two electrode stiffening rings. The stiffening rings and electrodes were made of molybdenum. The mounting ring attaches to a bracket at twelve points. For laboratory tests, twelve screws on the bracket join the bracket to the discharge chamber and center the electrodes on the axis of the chamber. For the structural analysis, the force transmitted through the brackets was assumed to be negligible. This allows the structural model of the assembly to be decoupled from a thruster model. The screen electrode has a hexagonal pattern of 0.19 cm diameter ion extraction holes on 0.22 cm centers (Fig. 3). The accelerator electrode is patterned similarly but with 0.11 cm diameter holes. The open area fraction of the screen and accelerator electrodes were 0.67 and 0.24, respectively. The insulator assembly consisted of two machine screws separated by a cylindrical piece of alumina which is drilled to permit outgassing (Fig. 2). The shadow shields over the alumina prevent shorts due to backsputtered material, and carry no structural load. A collar around the screws fixes the height of the accelerator electrode's stiffening ring and thus determines the initial electrode gap. Twelve insulators were positioned equally spaced around the edge of the accelerator electrode's stiffening ring.

Tests were conducted to measure the temperature distribution across the electrodes and mounting rings and the displacement of the center of the electrodes. A brief description of the apparatus follows and a more complete description can be found in reference 17. Thermocouples were mounted at 10 locations on the electrodes and mounting ring, as shown in Fig. 4. Temperatures

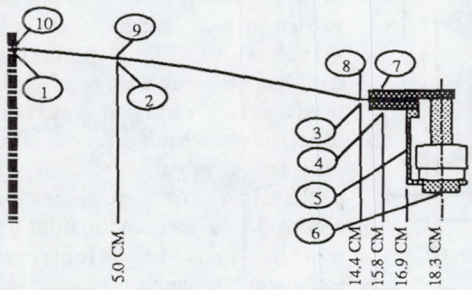

FIGURE 4. - THERMOCOUPLE LOCATIONS.

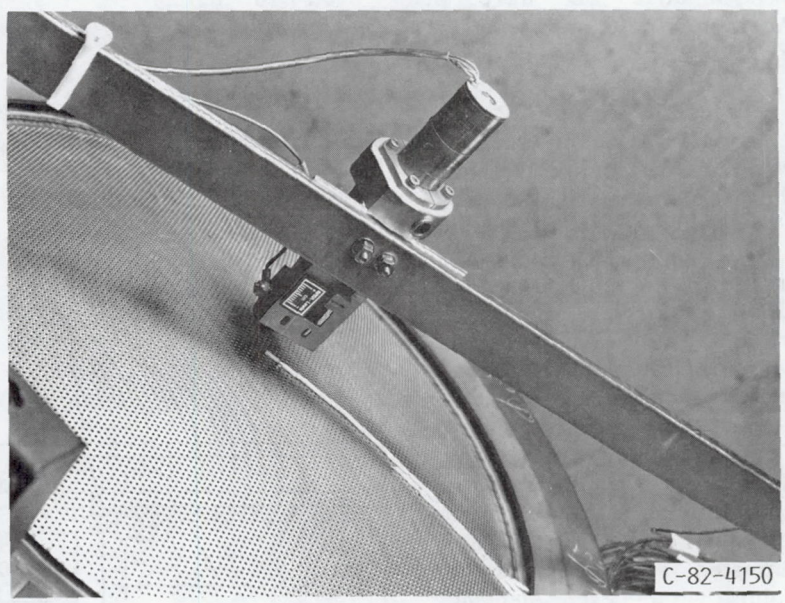

FIGURE 5. - DISPLACEMENT MEASURING PROBE.

TABLE II: TEMPERATURE AND DISPLACEMENT OF A J-SERIES ELECTRODE ASSEMBLY.					
Thermo-couple Location	Thermo-couple Number	Radial Position, cm	Temperatures, °C Discharge Power, W 210	350	450
Screen	1	0.0	278	353	397
	2	5.0	266	346	381
	3	14.4	194	294	324
Mounting Ring	4	15.8	191	291	319
	5	16.9	99	215	239
	6	18.3	83	196	216
	7	15.8	124	222	246
Accelerator	8	14.4	137	234	259
	9	5.0	189	276	310
	10	0.0	209	292	327
Centerline Gap Reduction, cm			0.0025	0.0051	0.0076
Centerline Screen Motion, cm			0.030	0.046	0.053
Centerline Accelerator Motion, cm			0.028	0.041	0.046

- Thermocouple numbers refer to Fig. 4.
- No ion beam extraction.
- Initial electrode gap was 0.051 cm.
- Data taken from Ref. 17.

were recorded as the electrodes heated. Two stepper motor driven probes were used to measure the displacement of the electrodes (Fig. 5). Equilibrium temperature and displacement measurements are listed in Table II. The probes were mounted on a bracket downstream of the electrodes (Fig. 6). Contact between a probe and the accelerator electrode or a probe and a post on the screen electrode completed an electric circuit. The motion of the electrodes was determined by the motion of the probe necessary to make and break contact with the electrodes.

MODELING APPROACH

All of the structural analysis was conducted by applying temperatures, and using boundary conditions to confine the motion of the edge of the electrode to the original plane, and confined motion of the center node to the axis of symmetry. The boundary conditions did not generate any load, so all forces and displacements were due thermal expansion and the geometry of the assembly. For the 3D Algor models, a 90° section was modeled (Fig. 7), and boundary conditions were applied to enforce radial symmetry, ie. no bending was allowed around the radial edges, and the nodes in the cutting planes were confined to motion in those planes.

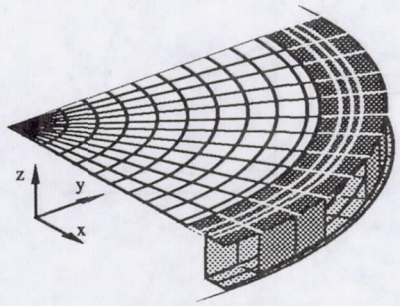

FIGURE 7. - J-SERIES 90° SECTION MODEL.

Four model configurations were examined to test the finite element

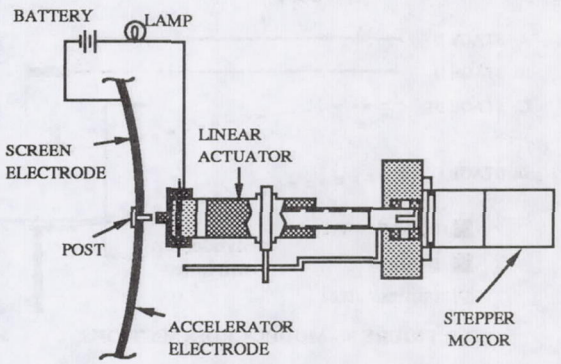

FIGURE 6 . - SCREEN ELECTRODE MEASURING SYSTEM SCHEMATIC.

codes and predict the behavior of the electrodes. The simplest model was compared to analytical solutions obtained using plate-shell theory.[23,24,25] Elements were then added to the model incrementally to observe their effects, and develop confidence in the model and methods used. Finally, the full mounting ring assembly was modeled and the predictions obtained by applying measured temperature gradients to the model were compared with measured displacements.

Configurations

Particulars of each of the configurations are given below. In order to reference the models easily, the models have been given codes, the first part is a Roman numeral indicating the stage or configuration modeled, a letter indicates the program used—a for Algor, m for MARC, and n for NASTRAN, and the Arabic number indicates whether the model used a 2D axisymmetric or 3D Cartesian coordinate system (Table III).

Flat Plate—Stage I A solid, flat, circular plate of molybdenum, 15 cm in radius, and 0.038 cm thick was the simplest model used (Fig. 8A). Analytical solutions are available from plate-shell theory for this geometry with radially varying temperatures loads.[18-20] This configuration represented the most complex problem with published solutions that contained any elements of the thruster model. The problem was modeled using all three codes. It was modeled with Algor in 2D axisymmetric coordinates and 3D Cartesian coordinates and was the only model used on NASTRAN.

Flat Plate with stiffening ring—Stage II A molybdenum stiffening ring was added to the Stage I model, extending from 15 cm to 18 cm radius,

TABLE III: LIST OF MODELS AND SOFTWARE USED				
	Flat Plate	Flat Plate with Stiffening Ring	Dished Plate with Stiffening Ring	Full Assembly
2D Algor	Ia2	IIa2	IIIa2	not modeled
3D Algor	Ia3	IIa3	IIIa3	IVa3
MARC	Im3	IIm3	IIIm3	not modeled
NASTRAN	In3	not modeled	not modeled	not modeled

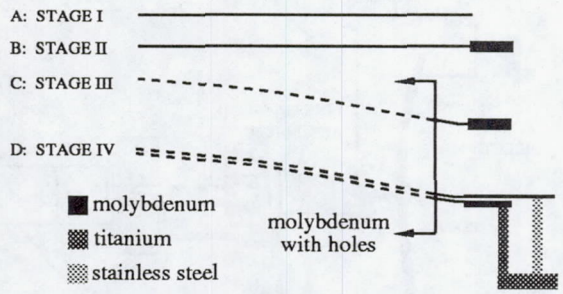

FIGURE 8. - MODEL CROSS SECTIONS.

0.318 cm thick (Fig. 8B). There were no published analytical solutions available for this geometry with a radially varying temperature load. The model was used with Algor in 2 and 3D and in 3D with MARC.

Dished Plate with stiffening ring—Stage III..With this model, the shape of the electrode is assumed to be a spherical surface section with a flat extension and a stiffening ring attached to the extension (Fig. 8C). The radius of curvature of the electrode is 48.2 cm which equates to a dish depth of 2.2 cm with a circle of 14.4 cm radius defining the edge.[21] The dimensions were altered slightly from the stage I and II models, a flat flange extends from 14.2 to 15 cm radius, and the stiffening ring from 15 to 16.6 cm. The dimensions describe the J-series screen electrode. The stiffening ring was 0.318 cm thick and the remainder of the model was 0.038 cm thick. The material properties were modified across the material inside a 14.2 cm radius to simulate different hole patterns, ie. no holes, 0.11 cm holes and 0.19 cm holes. Equations derived by Horvay[26] were used to modify the Youngs modulus (E) and the Poisson ratio (v) to account for the hole patterns,

$$E^* = (1-\nu^*)\frac{Eh_m}{C} \tag{4}$$

$$\nu^* = 1 - \frac{4}{3+2n(1+\nu)} \tag{5}$$

$$h_m = L\left[\int_0^L \frac{d\ell}{h}\right]^{-1} \tag{6}$$

where E^* is the effective Young's modulus, ν^* is the effective Poisson ratio, $2h_m$ is a mean ligament thickness, h is the instantaneous half-thickness of the ligament or web (Fig. 9), and n is a shape factor for the cross section of the ligaments, taken to be 1 for a rectangular cross section. The model was used with Algor in 2 and 3D and in 3D with MARC.

Unless otherwise stated, all of the data presented were computed with a Young's modulus of 280 GPa and a Poisson ratio of 0.324, corresponding to solid molybdenum, across the entire electrode.

30 cm Assembly with dished electrodes—Stage IV..The electrode assembly model was used only with Algor. The model builds on the Stage III model, using two dished electrodes connected by a circular, L-section mounting ring and insulators that were modeled with constant property plate elements (Fig. 8D). The dished electrodes used bulk material constants to simulate 0.19 cm diameter holes in the screen electrode and 0.11 cm diameter holes in the accelerator electrode. The mounting ring (Fig. 2) was modeled using material properties for titanium and a thickness of 0.10 cm. The plate elements used to model the insulators had a width of 10° at 18.3 cm radius and a thickness of 0.35 cm (Fig. 7). Using properties for cold rolled steel, the bending stiffness of the plate elements modeling the insulators was matched to the estimated stiffness of the spacing screws in the radial plane, necessarily making them stiffer in the circumferential plane. Except for the constraints on the circular edge, the same boundary conditions used with the other electrode models were applied to the stage IV model. Displacement constraints on the circular edge were applied only to the screen electrode. These boundary conditions are enough to eliminate rigid body motions without introducing additional stresses due to overconstraints, and results in all axial deformations being reported relative to the stiffening ring on the screen electrode.

RESULTS

The results of the computer models were checked for sensitivity to the meshing and input parameters, agreement between different programs, and continuity with the other models. The output from the stage I model was compared with analytical predictions from plate-shell theory. The predictions from the stage IV electrode assembly model were compared with measured

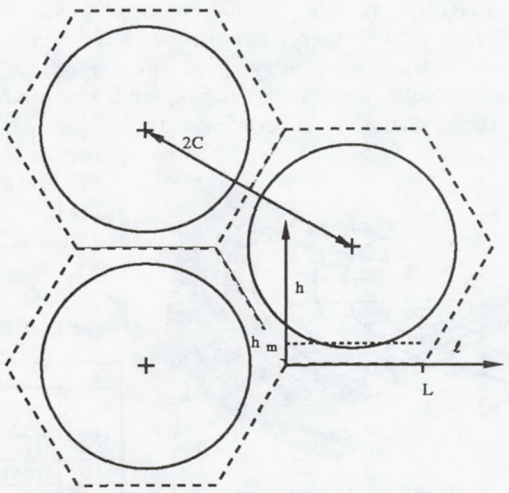

FIGURE 9. - HOLE GEOMETRY AND DEFINITIONS.

displacements. The stage II and III models were transitional stages between the stage I and IV models.

Input Sensitivity

In finite element modeling, the level of detail incorporated in a model must be balanced against the numerical accuracy of the program, and the time required to generate results. The objective of this sensitivity analysis was to evaluate the meshing options and the number of nodes for accuracy and computational efficiency and to evaluate the effect of varying inputs like temperature gradients and material constants.

Evaluation of meshing Each element in a model is defined by its nodes. The 2D axisymmetric elements each have two nodes, one at each end point. The 3D elements used have four nodes each, defining the corners of a quadrilateral. The number of nodes determines computer time required and, to a large extent, the accuracy of the model. The model must have enough nodes to approximate the shape of the stress and displacement distribution. However, as the node spacing decreases, truncation errors become more noticeable and the computer time required increases.

The results of IIIa2 models with 5, 10, 20 and 30 nodes across the electrode were compared. The number of elements in each 2D model was one less than the number of nodes. Displacement predictions using 10, 20 or 30 nodes are within 0.1% of each other, but 5 node predictions diverge along the centerline and at the edge (Fig. 10). Stress

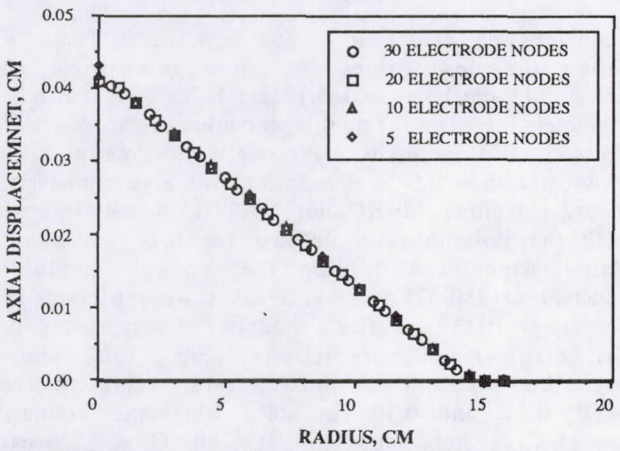

FIGURE 10. — VARIATION IN DISPLACEMENT PREDICTIONS WITH MODEL SIZE, IIa2 MODEL.

predictions from the 10, 20 and 30 node models were also within 0.1% and the 5 node model predictions diverged along the centerline.

With 3D models, appropriate meshing must be chosen in the radial direction and in the azimuthal direction. Runs with circumferential spacings of 15°, 10°, 7.5°, 5° and 2.5° showed no difference in either stress or displacement predictions. A 5°

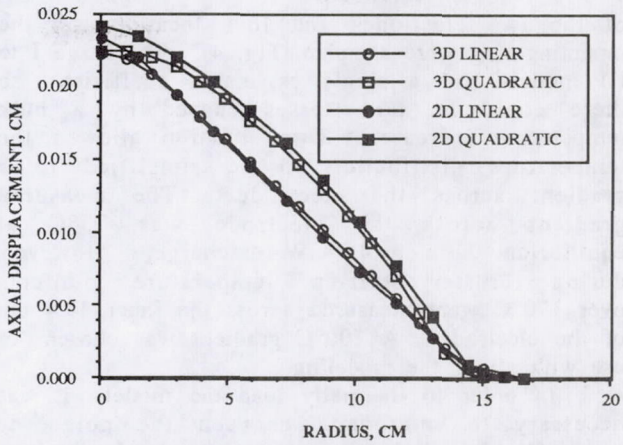

FIGURE 11. — DISPLACEMENT DUE TO IMPOSED TEMPERATURE GRADIENTS, STAGE III MODEL.

spacing was chosen for all of the 3D models because it had the flexibility needed to model the insulators on the stage IV assembly model and required less than two hours to execute on an IBM PC.

The 3D models were tested with 10, 15 and 20 radial nodes on Algor and MARC. Close agreement was seen with the 2D axisymmetric predictions except along the centerline (Fig. 11). The 3D models consistently predicted less displacement of the center elements than the 2D models predict. The deviation is due to the formulation of triangular elements which are used in the center, and will be discussed in the plate-shell theory section.

There is an additional choice to be made with the 3D models. The full assembly can be modeled with a 90° section (Fig. 7) by using boundary conditions to enforce the axial symmetry of the full model. The boundary conditions are simple when the X-Z and Y-Z planes are used to section the model, and good agreement with a full 360° model was found by Brophy[13] using Algor. Using the 90° section, the number of nodes can be reduced by nearly a factor of four. Because computer time increases with the square of the number of nodes, the time required can be reduced by about a factor of 15. The drawback is that only axisymmetric buckling can be modeled using a 90° section. The stage III, 90° section Algor models required about 40 minutes to converge. The 360° MARC and NASTRAN models required less than one minute of CPU time on the Cray, so they were not modeled as 90° sections.

Temperature gradient sensitivity The only load applied to the model was a temperature distribution. The differential thermal expansion across each electrode caused stresses and deflections. Because the ultimate goal of the modeling was to predict the behavior of the electrodes without knowing the exact temperature distribution, one must know how the shape of the temperature function affects the prediction.

Data were taken previously at ten locations on the electrode assembly.[17] Three locations on each

of the two electrodes and four locations on the mounting ring were sampled (Fig. 4). The Stage I to III models had a single expansion coefficient, so there could be no stresses caused by a bulk temperature increase. This situation allowed the temperature distribution to be simplified to a gradient across the electrode. The measured gradient across the electrode was 73°C at equilibrium with a 450 W discharge. However, during thruster start-up, temperature gradients over 170°C were measured across the inner 14.4 cm of the electrode. A 100°C gradient was chosen for use with all of the modeling.

In order to thermally load the models, it was necessary to interpolate between the points to generate data at the coordinates the model required. Three different profiles were used to model the thermal load. The simplest temperature profile used was linear, ie 100°C at the electrode center to 0°C at 14.4 cm radius. The next profile was a quadratic curve that was fit to the three data points available for the screen electrode at 450 W equilibrium temperatures (Ref. 17). The fitted curve was then normalized to 100°C at the center and 0°C at 14.4 cm radius. Neither of these profiles reflect the physics of heat transfer, they merely fit the limited data available and the constraints chosen. The constants that were found are given in Table IV.

TABLE IV: TEMPERATURE DISTRIBUTION EQUATIONS

Equation Form	A	B	C
$T(°C) = A + Br$	100	-6.94	——
$T(°C) = A + Br + Cr^2$	100	-3.02	-0.272

The third method of interpolating between the data available was used only with the stage IV, full assembly model. A cubic spline was fit to the data. The method and results are described below, in the section comparing the model results to the measured displacements.

Both gradients from Table IV were applied to the stage three models. The results show less than 3% variance for the displacement at the center, with measurable differences near the mid-radius. The quadratic distribution generated about 33% more displacement at the mid-radius than the linear profile caused (Fig. 11).

Evaluation of material constant effects In order to model the perforations of the electrodes, bulk material constants were calculated for the modified molybdenum sheet. Equations 4 through 6 were used[27] to calculate appropriate values of Young's modulus and Poisson ratio. The equations define the new properties based on the hole

TABLE V: MATERIAL PROPERTIES USED TO MODEL PERFORATED MOLYBDENUM SHEET.

Geometry	E* GPa	v*	Open Area Fraction
no holes	280	0.32	0
0.11 cm holes	47	0.33	0.24
0.19 cm holes	8.1	0.62	0.67

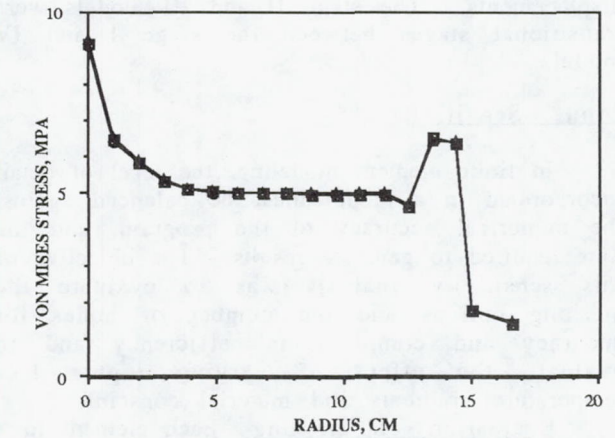

A. — DISPLACEMENT VARIATIONS.

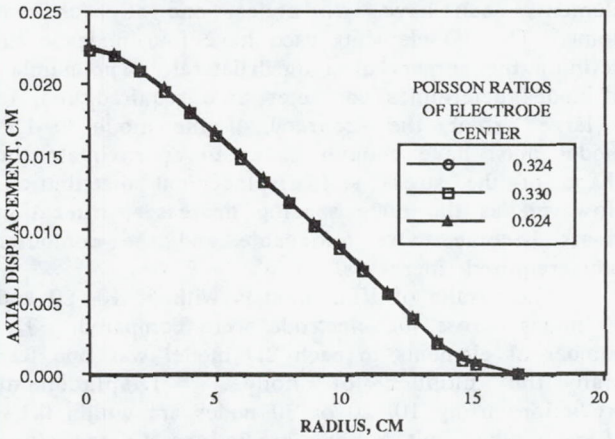

B. — STRESS VARIATIONS

FIGURE 12. — SENSITIVITY TO POISSON RATIO, MODEL IIIa3.

diameter and center to center spacing. Table V shows the new values for three geometries, no holes, 0.11 cm holes and 0.19 cm holes. As the hole diameter increases, Young's modulus decreases and Poisson ratio increases. Physically, a Poisson ratio of greater than 0.5 is nonsensical for elastic material theory. Neither MARC nor NASTRAN will operate with the Poisson ratio defined for 0.19 cm holes. Using Algor and holding the Young's modulus constant at 280 GPA, several cases were tried using the stage IIIa3 and IIIa2 models. Comparisons of the displacement predictions (Fig. 12a) show negligible variation for Poisson ratios representative of 0, 0.11, and 0.19 cm holes when the Young's modulus is held constant at 280 GPa. Stress variations (Fig. 12b) are also negligible. The von Mises stress is a root mean square of the principal stress magnitudes that provides a simple means of comparing the stress vectors.

There was also some question about the necessity of varying Young's modulus. Provided that there are no geometric or material nonlinearities in the structure, the Young's modulus should make little difference in the magnitude of the displacement. Indeed, for very simple structures, the Young's modulus drops out of the

equation for displacement (see Eq. 10). But, when one adds materials with different thermal expansion rates, the system becomes nonlinear. Additionally, one of the goals of the modeling efforts is to simulate nonlinear effects due to plastic strain. This requires accurate stresses and more material information than is currently available. Holding the Poisson ratio constant at 0.324, the IIIa3 model was tested with Young's moduli of 280, 47 and 8.1 GPa for the perforated region of the electrodes. The prediction of the magnitude of the maximum stress is strongly affected by the value of Young's modulus chosen (Fig. 13). Because there was little difference in the radial motion of the nodes on the stiffening ring, there is little difference in the electrode displacement predictions.

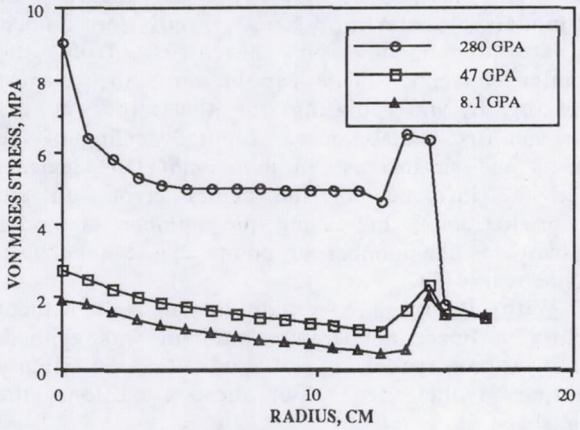

FIGURE 13. — SENSITIVITY OF STRESS PREDICTIONS TO YOUNG'S MODULUS, MODEL IIIa3.

When the Horvay modifications to the material constants were examined separately, stress and deflection were found to be undisturbed by changes in Poisson ratio, but Young's modulus strongly affected the stresses.

Comparison of Results with Plate-Shell Theory

Thermal stress and deformation equations have been published for flat circular plates with arbitrary axisymmetric temperature gradients.[25] The analyses describe stresses that occur when buckling is not allowed, and deformations for buckled cases. These analyses are compared to the predictions of the finite element programs for the same conditions. Comparisons of the stress predictions for an unbuckled flat plate allow a direct check on the stress predictions of the codes. The stress is directly coupled to the displacement through Hooke's Law, and correct evaluation of the stress is important for future analyses involving non-linear material properties and plastic deformation. The displacement predictions were checked by comparing buckling mode shape equations[25] with the eigenvalues generated by the model.

Without buckling For these analyses, a linear temperature gradient, with a maximum temperature of 100°C at the center and 0°C at 15 cm, was used. This gradient causes stresses to develop due to the geometry of the plate. The equations allow only radial motion of the points within the plate. The material stresses generated under these conditions are:

$$\sigma_r = \frac{\alpha E \Delta T}{3R}(r - R), \tag{7}$$

$$\sigma_c = \frac{\alpha E \Delta T}{3R}(2r - R), \tag{8}$$

and

$$S = \frac{\alpha E \Delta T}{3R}\sqrt{3r^2 - 3rR + R^2}, \tag{9}$$

where σ_r and σ_c are the stresses in the radial and circumferential directions respectively, ΔT is the temperature difference between the center and edge, and S is the von Mises averaged stress.[23] For the following Stage I modeling, a Young's modulus of 8.1GPa and a Poisson ratio of 0.324 were used.

The stage I models are equivalent to the system modeled by Goodier[24]. The temperature difference was applied across the plate using all three finite element codes (Fig. 14). The Ia2 model agrees with the closed form theoretical analysis. All of the 3D analyses show errors at the center and smaller errors at the periphery. The error at the edge was deemed insignificant, but, because the region of most deflection and first likely contact is the center of the electrode, improvements to the center node stress predictions were sought.

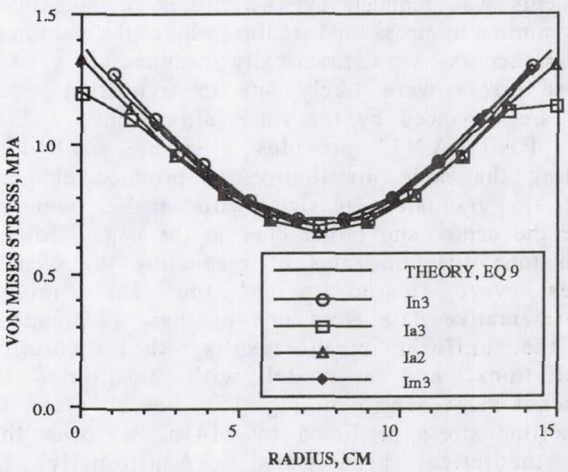

FIGURE 14. — COMPARISON OF FLAT PLATE STRESS PREDICTIONS WITHOUT BUCKLING, STAGE I MODEL.

The reduced stress that the 3D codes predict at the center of the plate is a fault in the formulation of the triangular elements and is common to all 3D stress codes.[27] Several methods of reducing the effect of this error have been investigated. When the size of the triangular

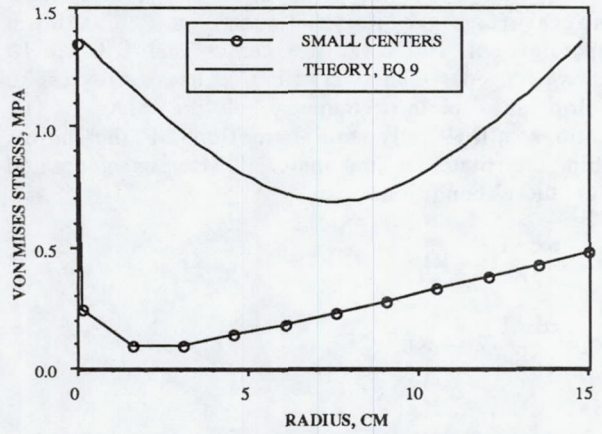

FIGURE 15. - STRESS PREDICTION WITH SMALL CENTER ELEMENTS, MODEL Im3.

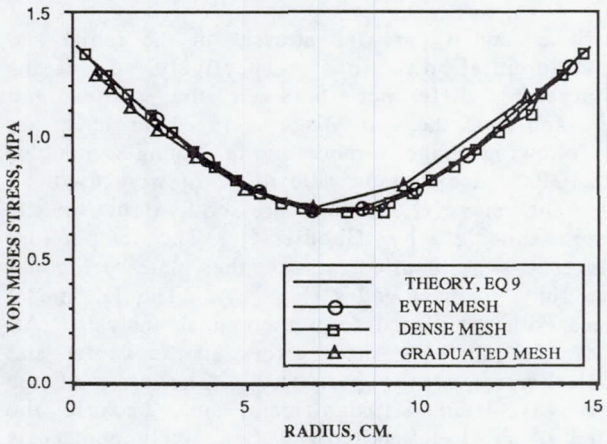

FIGURE 16. — STRESS PREDICTION VARIATIONS WITH NODE DISTRIBUTION, MODEL Im3.

elements was reduced by two orders of magnitude, the minimum stress and radius where the minimum stress occurs were drastically reduced (Fig. 15). These errors were likely due to truncation errors that are enhanced by the small dimensions.

PATRAN[19] provides a simple method of scaling the node distribution to produce elements that are graduated in size, with smaller elements near the center and larger ones at the edge. Models with four different rates of graduating the element sizes were tested using the Im3 model. Representative data from one of these is compared to the uniform mesh results, the theoretical predictions, and a model with 2.5 times the standard mesh density in Fig. 16. For all cases, the centerline stress predicted by MARC is lower than the theoretical predictions. Additionally, the minimum stress and point of minimum stress is incorrectly predicted when the element size is graduated. For the even, dense and graduated meshes, the stress predicted by the models was within 10% of the stress predicted with plate-shell theory.

An early attempt at a solution was combining pairs of center triangles to make quadrilateral elements. The large angle that results along the circumference of the element leads to computational inaccuracies for the quadrilateral elements. These errors affect stress predictions past the mid radius, and destroy the azimuthal symmetry, making post processing more tedious. For these reasons, center quadrilaterals were deemed an unworkable solution.

Over all, the accuracy of the models is good when neighboring elements are of comparable size. The model consists primarily of quadrilateral elements and, although the stress from the triangular elements affects the loading of the quadrilaterals, the stress predicted just two nodes away from the center is within 5% of the theoretical value. Any method of improving the accuracy of the models' centerline stress predictions must eliminate dependence on the stress from the triangular elements. This can be done in the post processing by interpolating for the stress at the center and first radial nodes. Limited scaling of the elements and an increase in the number of elements reduce the influence of the center errors on the bulk predictions. Increasing the number of nodes also increases the number of points that can be used with the curve fit.

With Buckling As with the analysis without buckling, a linear temperature gradient was applied. The equations model a flat plate that is simply supported at the edge. For these conditions, the mode shape is

$$w=\frac{\alpha\Delta T}{t}\left[(9r^2R-4r^3-5R^3)\frac{(1+\nu)}{36R}-(r^2-R^2)\frac{(1-\nu)}{12}\right] \quad (10)$$

where w is the displacement perpendicular to the plate[25]. The Poisson ratio must be less than 0.5 for this equation to hold. From the displacement function, the stress function can be calculated. The resulting stress is

$$S=\sigma_a=\frac{Et^2\alpha\Delta TR}{9}(R-r) \quad (11)$$

where the only component is shear in the axial direction, σ_a, so the von Mises stress equals the shear stress.

All three programs are capable of solving for the buckled mode shape. However only MARC was used to solve for the buckling mode. Comparison of the computed and analytical mode shapes (Fig. 17) shows reasonable agreement everywhere. The buckling solution is given by solving for the eigenvalues and eigenvectors of the generalized stiffness matrix. MARC normalizes the resulting eigenvector to one. Because the greatest deflection occurs at the center node, the center node solution must agree with theory. The fact that all of the other nodes also show good agreement with theory suggests that the solution at those points will not be strongly affected by the triangular element errors.

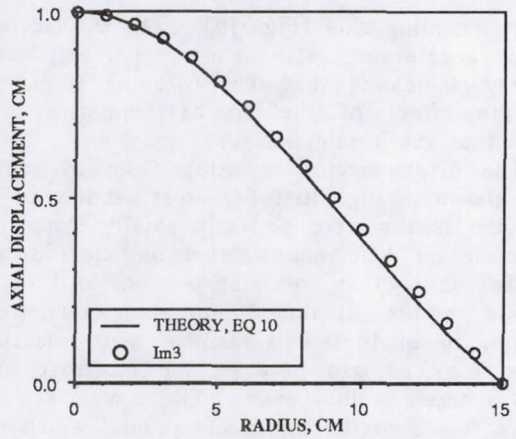

FIGURE 17. — COMPARISON OF PREDICTED BUCKLING MODE SHAPES, MODEL Im3.

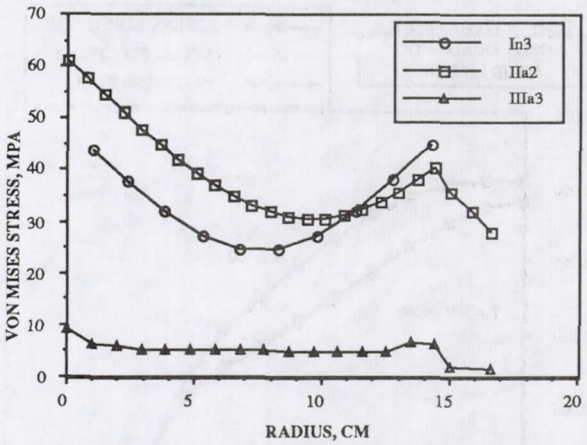

FIGURE 18. — COMPARISON OF STAGE I, II AND III RESULTS MODELING ELECTRODES PERFORATED WITH 0.19 CM HOLES.

Transitional Configuration (II and III) Results

Configurations II and III were used on Algor and MARC in order to build confidence in the similarity of the programs' output and link the analytically verifiable work to the experimentally verifiable in steps that permit an intuitive check on the model results. With the level II models, a stiffening ring was added to the flat plate. The stage III models incorporate the dished structure of the J-series electrodes and the stiffening ring from the stage II model. The models were loaded with a linear temperature gradient normalized to 100°C. Results are compared in Fig. 18. The stage II structure shows higher centerline stresses than the stage I structure and the minimum stress on the electrode occurs at a larger radius. The shape of the stress distribution across the electrode is quadratic for both stage I and II. The stage II stress distribution departs from the quadratic form at 15 cm, where the stiffening ring begins. The stage III structure deflects axially without the use of the buckling solution. The deflection allows a large reduction in the stress throughout the model. The sharp changes in the stress values at 15 cm radius is due to a change in thickness. The stage II and III models produced no inexplicable displacements or stresses.

Comparison of Model IVa3 with Engine Data

Algor was used for the full electrode assembly model because it allowed direct access to the stiffness matrix parameters through the pre-processor, simplifying the temperature loading. A choice had to be made in representing the insulators (Fig. 2). It seemed that one dimensional pin elements would be the best option, so they were tried first. The program would not execute when pins were used in the 3D structure, so the model was rebuilt with 2D plate elements simulating the insulators. The program executed , but it is more difficult and less accurate to model an axisymmetric insulator with a single plate shell element rather than a pin element.

Simple, linear and quadratic temperature profiles (Table IV), applied to the Stage I to III electrode models, were applied to the Stage IV assembly model to provide a basis for comparison. However, the Stage IV model includes materials with different expansion coefficients and therefore, the possibility of stresses generated by constant temperature loads arises. The simple temperature distributions from Table IV do not model the temperature distribution across the mounting ring, nor do they model the bulk temperature increase. To handle these additional conditions, a cubic spline was fit to the temperature data.[17] The coordinates of the test data were converted to a path length along a cross section in order to reflect the path of thermal conduction. The path defined runs from the center of the screen electrode, through the mounting ring to the center of the accelerator electrode. A standard spline routine from the IMSL/Math subroutine library, CSAKM,[28] was chosen to minimize oscillations in the resulting curve. The equations generated are shown in Table VI.

TABLE VI. — SPLINE FIT TO TEMPERATURE DATA.

POSITION	FOR r BETWEEN	AND	FOR s BETWEEN	AND	TEMPERATURE, °C
SCREEN	0.0	5.0	0.0	5.0	$397-1.831s-0.254s^2-0.004s^3$
	5.0	14.4	5.0	14.6	$381-4.668(s-5.0)-0.283(s-5.0)^2+0.016(s-5.0)^3$
MOUNTING RING	14.4	15.8	14.6	16.0	$324-5.755(s-14.6)+4.843(s-14.6)^2-2.345(s-14.6)^3$
	15.8	16.9	16.0	18..2	$319-5.984(s-16.0)-37.832(s-16.0^2+10.920(s-16.0)^3$
	16.9	18.3	18.2	21.7	$239-13.891(s-18.2)+1.583(s-18..2)^2+0.145(s-18..2)^3$
	18.3	15.8	21.7	29.0	$216+2.529(s-21.7)-0.084(s-21.7)^2+0.041(s-21.7)^3$
	15.8	14.4	29.0	30.4	$246+7.882(s-29.0)+4.077(s-29.0)^2-2.196(s-29.0)^3$
ACCELERATOR	14.4	5.0	30.4	40.4	$259+6.384(s-30.4)-0.089(s-30.4)^2-0.002s-30.4)^3$
	5.0	0.0	40.0	45.0	$310+4.021(s-40.0)-0.057(s-40.0)^2-0.013(s-40.0)^3$

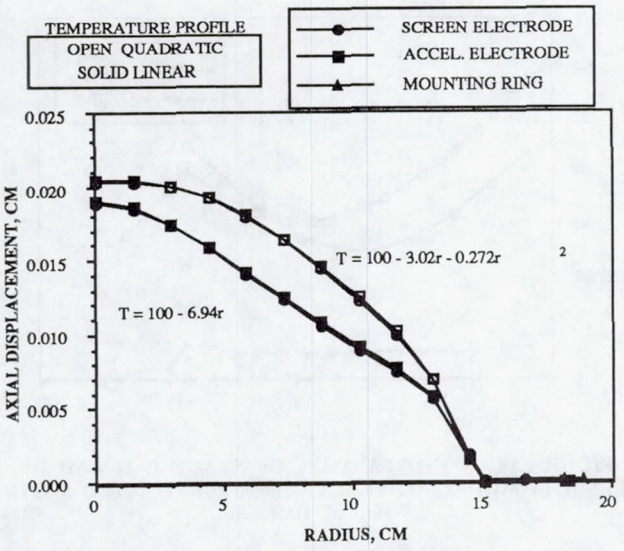

FIGURE 19. — ELECTRODE MOTION WITH SIMPLE TEMPERATURE GRADIENTS, MODEL IVa3.

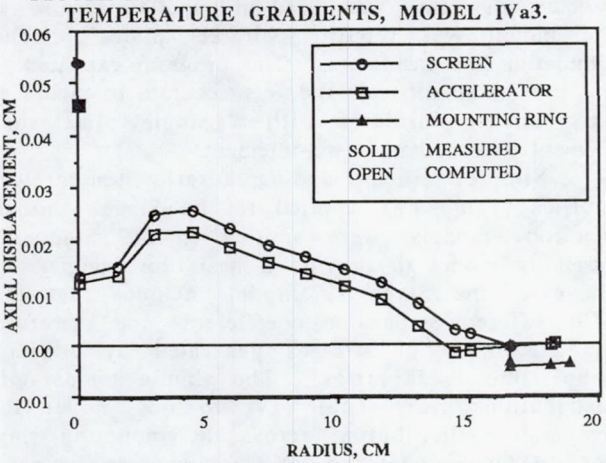

FIGURE 20. — DISPLACEMENTS WITH MEASURED TEMPERATURE GRADIENT, MODEL IVa3.

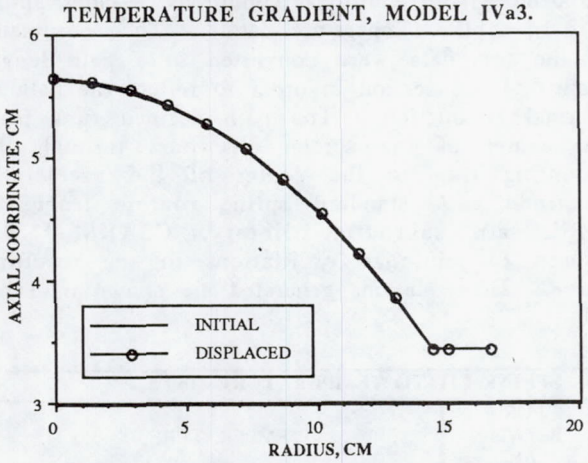

FIGURE 21. — DISPLACED SHAPE COMPARISON, MODEL IVa3.

The results obtained using the simple linear and quadratic temperature gradients (Table IV) show identical motion of the screen and accelerator electrodes, indicating that the stiffening rings completely mask the effect of the expanding, titanium mounting ring (Fig. 19). The displacement of the accelerator also shows perfect, axial symmetry, indicating that the stiffening rings also mask the effect of the non-axisymmetric loads generated at the insulators.

The displacements resulting from the spline fit are shown in Fig. 20 for a cross section at 30°. Again, the results were perfectly axially symmetric, so it made no difference whether the cross section was taken through an insulator or not. All of the electrode nodes displaced in the downstream direction, in qualitative agreement with measured results.[17] The gap between the electrodes was slightly reduced at the center. The center is shown to move less than the mid-radial points, which may be somewhat misleading. Because the electrodes are initially dished more than 2 cm, there is no reversal of the electrode curvature. In fact, a scaled plot showing the initial and final states (Fig. 21) shows no discernable displacement.

Although the triangular elements still affect the displacements, the results from applying simple gradients (Table IV) show the maximum displacement occuring at the center (Fig. 19). Therefore, one must conclude that the reduced central displacement that the spline loaded model shows is due to the temperature gradient applied and not to the triangular element errors that plague the analyses. This conclusion suggests two possibilities, the electrodes may deflect in such a fashion, or the temperature load that causes such deflection is in error. More detailed experimental measurements of temperature and displacement could prove conclusively which is true.

CONCLUDING REMARKS

Three finite element codes were used to analyze the thermo-mechanical response of ion engine electrodes to various input parameters. The codes were compared with each other to examine the sensitivity to meshing choices and the differences between 2D axisymmetric and 3D models. The effects of applying different temperature profiles to the models were examined. The sensitivity of the stress and displacement predictions to Young's modulus and Poisson ratio changes was examined to determine what material constant adjustments are necessary to model perforated molybdenum. The model predictions were compared with plate-shell theory predictions to evaluate the accuracy of the 2D and 3D results. In order to develop an intuitive understanding and continuity between simple plate-shell structures and a full thruster model, models with single electrodes and stiffening rings were used. Finally, results from a three dimensional model of the electrode assembly were compared to measured displacements.

Several conclusions can be drawn from the work completed. Models with sufficient node

density to provide consistent electrode stress and displacements were demonstrated on both mainframe and personal computers.

The shape of the temperature gradient applied affects the off axis displacements measurably. This means that reasonably accurate temperature distributions must be developed, through modeling or measuring, in order to analyze new designs.

Perforated sheet can be modeled as solid by changing the Young's modulus, Poisson ratio and yield stress. Yield stress sensitivities were not examined because no data beyond yield were available. Accurate values of Young's modulus were essential for modeling perforated material; both stress and displacement predictions were affected. Poisson's ratio was shown to have negligible effect on stress and displacement profiles. If the models are to be expanded to include plastic strain and other non-linear, non-isometric effects, materials testing to determine the properties is necessary.

The two dimensional, axisymmetric models agree well with plate-shell theory. The 3D models all have errors where triangular elements are used. The errors are due to constant strain formulation of the triangular elements and cannot easily be eliminated. In spite of errors from the triangular elements in the 3D models, the displacement and stress predictions from the quadrilateral elements are very close to closed form solutions for flat plates.

Qualitatively, displacement predictions made by the models agree with measured displacements, showing both electrodes moving downstream with the screen electrode moving further than the accelerator electrode. The existing experimental database is insufficient for strong quantitative comparisons to be made. Structural finite element models of ion engine electrodes are in a state of readiness. Further development and useful output await detailed experimental measurements.

ACKNOWLEDGEMENTS

The assistance of Brian Fite and Jay Malloy in learning to use the finite element codes, MARC and PATRAN in particular, was invaluable. Much of the work completed would not have been possible without them.

REFERENCES

1. Stone, J. R., Byers, D. C. and King, D. Q., "The NASA Electric Propulsion Program," Proceedings: 20th International Electric Propulsion Conference, October 1988, pp. 17-25.

2. Sponable, J. M. and Penn, J. P., "Electric Propulsion for Orbit Transfer: A Case Study," Journal of Propulsion and Power, Vol. 5, No. 4, July 1989.

3. Palaszewski, B., "Electric Propulsion for Manned Mars Exploration," Proceedings: 1989 JANNAF Propulsion Meeting, Vol. 1, May 1989, pp. 421-35.

4. Forester, T. A., Large Ion Beams: Fundamentals of Generation and Propagation, John Wiley and Sons, Inc., New York, 1988.

5. Rawlin, V. K. and Patterson, M. J., "High Power Ion Thrusters," NASA TM 100127, Jan 1987.

6. Rawlin, V. K., "Studies of Dished Accelerator Grids for 30 cm Ion Thrusters," AIAA Paper 73-1086, October, 1973.

7. Lathem, Walter C., "Approximate Analysis of the Effects of Electrode Misalignments on Thrust Vector Control in Kaufman Thrusters," AIAA Paper 68-89, January, 1968.

8. Aston, G. and Brophy, J. R., "A 50 cm Diameter Annular Ion Engine," AIAA Paper 89-2716, July, 1989.

9. Kaufman, H. R., and Robinson, R. S., "Industrial Ion Source Technology," NASA CR 159887, Dec. 1979.

10. Rawlin, V. K., Millis, M. G., "Ion Optics for High Power, 50 cm Diameter Ion Thrusters", AIAA Paper 89-2717, July, 1989.

11. Poeschel, R. L. and Kami, S., "Analysis and Design of Ion Thrusters for Large Spacecraft Systems," NASA CR-165140, September 1980.

12. James, E. L., et al, "Advanced Inert Gas Ion Thrusters," NASA CR-1618912, July 1984.

13. Brophy, J. R. and Aston, G., "Thermal Mechanical Analysis of Large Diameter Ion Accelerator Systems," AIAA Paper 89-2718, July 1989.

14. Algor Processor Reference Manual, Algor Interactive Systems, Pittsburgh, August 1989.

15. Berry, Dale T., "Beyond Buckling: A Nonlinear F. E. Analysis," Mechanical Engineering, August 1987, pp 40 - 44.

16. NASTRAN Users Manual, Vol. 1 & 2, MacNeal-Schwendler Corporation, Los Angeles, December 1981.

17. MacRae, G. S., Zavesky, R. J. and Gooder, S. T., "Structural and Thermal Response of 30 cm Diameter Ion Thruster Optics," AIAA Paper 89-2719, July 1989.

18. MARC User Information Manual, Vol. A, Rev. K3, MARC Analysis Research Corporation, July 1988.

19. PATRAN Users Guide, Vol. 1 & 2, Release 2.0, PDA Engineering, Santa Anna, December 1985.

20. MacNeal, R. H., ed., Handbook for Linear Static Analysis, MacNeal-Schwendler Corporation, Los Angeles, December 1981.

21. "30 Centimeter Ion Thrust Subsystem Design Manual," NASA TM-79191, June 1979.

22. Ogleby, J. C., "Thermal Analytical Model of a 30 cm Engineering Model Mercury Ion Thruster," NASA TMX 71680, 1975.

23. Young, W. C., Roark's Formulas for Stress and Strain, 6th Ed., McGraw Hill, New York, 1989.

24. Goodier, J. N., "Thermal Stress," Journal of Applied Mechanics, vol. 4, no. 1, March, 1937.

25. Goodier, J. N., "Thermal Stress and Deformation," Journal of Applied Mechanics, vol. 24, no. 3, September, 1957.

26. Horvay, G., "The Plane Stress Problem of Perforated Plates," Journal of Applied Mechanics, vol. 19, pp. 355-360, Sept. 1950.

27. Zienkowiecz, O. C., The Finite Element Method, 3rd Ed., McGraw Hill, London, UK, 1977.

28. IMSL Math/Library: FORTRAN Subroutines for Mathematical Applications, Ver. 1.0, IMSL, Houston, Texas, 1987.

NASA
National Aeronautics and Space Administration

Report Documentation Page

1. Report No.	2. Government Accession No.	3. Recipient's Catalog No.
NASA TM-103618 AIAA-90-2649		

4. Title and Subtitle	5. Report Date
Status of Structural Analysis of 30 cm Diameter Ion Optics	
	6. Performing Organization Code

7. Author(s)	8. Performing Organization Report No.
Gregory S. MacRae and Gary T. Hering	E-5775
	10. Work Unit No. 506-42-31

9. Performing Organization Name and Address	11. Contract or Grant No.
National Aeronautics and Space Administration Lewis Research Center Cleveland, Ohio 44135-3191	
	13. Type of Report and Period Covered Technical Memorandum

12. Sponsoring Agency Name and Address	14. Sponsoring Agency Code
National Aeronautics and Space Administration Washington, D.C. 20546-0001	

15. Supplementary Notes

Prepared for the 21st International Electric Propulsion Conference cosponsored by the AIAA, DGLR, and JSASS, Orlando, Florida, July 18-20, 1990.

16. Abstract

Three structural finite element programs are compared with theory, experimental data, and each other to evaluate their usefulness for modeling the thermomechanical deflection of ion engine electrodes. Two programs, NASTRAN and MARC, used a Cray XMP and the third, Algor, used an IBM compatible personal computer. The shape of the applied temperature gradient greatly affects off-axis displacement, implying that an accurate temperature distribution is required to analyze new designs. The use of bulk material constants to model the perforated electrodes was investigated. The stress and displacement predictions are shown to be sensitive to the temperature gradient and the Young's modulus, and insensitive to number of nodes, above some minimum value, and the Poisson ratio used. The models are shown to be useful tools for evaluating designs. Experimental measurement of temperatures and displacements was identified as the most critical area for further work.

17. Key Words (Suggested by Author(s))	18. Distribution Statement
Electric propulsion Ion beams	Unclassified – Unlimited Subject Categories 20 and 39

19. Security Classif. (of this report)	20. Security Classif. (of this page)	21. No. of pages	22. Price*
Unclassified	Unclassified	17	A03

NASA FORM 1626 OCT 86

*For sale by the National Technical Information Service, Springfield, Virginia 22161